Geometric model of UVIS window ghosts in WFC3

P. McCullough

ABSTRACT

We provide a geometric model for four specific ghost reflections in WFC3 UVIS. The model predicts a) the locations, shapes, and surface brightnesses of the ghosts of bright stars, and b) the location, shape, and brightness of a wedge-shaped feature apparent in flat fields obtained during ground testing using CASTLE stimulus at GSFC, and in flight by illuminating the CCDs with the moonlit Earth. This feature is also apparent in low-frequency flat fields derived from photometric analysis of stars which have been dithered across the field of view (a.k.a. L-flats). Stiavelli (2001) predicted the ghosts from ray tracing; the contribution of this report is to analyze the properties of observed ghosts and their effects on flat fields. In particular, ghost reflections create a wedge-shaped feature in flat fields due to light reflected from the detector returning to the detector chamber's window, and then back to the detector. We also outline potential improvements to the process of generating flat fields in the presence of such ghosts. In filter F606W, a V=15.0 solar-type star located so as to maximize the visibility of its window ghosts will produce four separate ghosts that respectively are 62%, 43%, 6%, and 4% as bright as the sky with average zodiacal and earthshine contributions. For a grid of stellar positions across quadrant D, we tabulate the V band magnitudes of stars that produce ghosts 10% as bright as the sky in F606W. Finally, we created an XML-formatted file that observers may use within the graphical user interfaces of APT and Aladin to estimate the location of the ghosts in any UVIS field of view or orientation.

Introduction

Ghost reflections occur in WFC3 due to reflections surfaces of transmissive optics, particularly the filters and the two windows over the CCDs. Because the filter ghosts originally were too strong (Brown & Lupie 2004), new filters were installed, which reduced the ghosts attributable to filters (Brown 2007a). Throughout this report, we do

not discuss filter ghosts; the only optical ghosts discussed are those generated by light reflecting from WFC3's UVIS tilted focal plane, back to the detector's two windows, and finally returning to the silicon CCD (Figures 1 and 2). Because we do not discuss any other ghosts in this report, we do not repeatedly identify the ghosts as "detector-window ghosts," but here alert the reader that is what we mean in all cases.

The ghosts are illustrated in the WFC3 Instrument Handbook (WFC3 IHB Figure 6.9 of the star cluster 47 Tuc refers to them as "figure-eight window ghosts") and in a WFC3 website[1] (under the heading "optical ghosts"). More examples are illustrated in this report: some of which we obtained from non-proprietary (as of February 2011) Hubble Legacy Archive quick look images with filters F606W or F814W from the following programs: 11700, 11724, 11803, 11924, and 12077. Program 11924 had many examples.

The ghosts' effect on flat fields is to create a wedge-shaped feature extending approximately from the middle of quadrant D upward and to the left into quadrant A (see Figure 5.3 of the WFC3 IHB). In prior work, the effect of these ghosts on flat fields was evident already (see Figures 1-3 of Bushouse 2005) and known to occur through many different filters (see Figure 5 of Baggett 2005). Bushouse (2005, also as cited by Brown 2007b) had identified the summation of ghosts as a cause of the lower-right-hand half of a "diamond-shaped pattern" in WFC3 UVIS flat fields (see Brown's Figure 12). Although the other half of the "diamond" was identified as glints from baffles and eliminated by careful masking, the ghost-generated "wedge" discussed here could not be eliminated so easily.

For the WFC3 UVIS detector, the relative tilt of the detector with respect to its (plane-parallel, flat, fused silica) window is reported to be ~20º or 21º according to Stiavelli et al. (2001) and the WFC3 IHB, respectively.[2] Side-view, scale drawings of the UVIS enclosure are in Figures 45 and 100 of Fineberg (2009). The window tilt angles for WFC3 UVIS and ACS WFC and are approximately equal[3], and they both exhibit these ghosts, which implies that their window-to-detector separations must be approximately the same. Incidentally, a relative tilt angle between detector and its window equal to 30º would prevent all detector-window ghosts from landing on the detector, even for a tiny detector-window minimum separation, because light rays from such ghosts will travel parallel to the detector plane.

Below we discuss the locations, shapes, and brightnesses of ghosts of stars, and then ghosts of flat fields. Although we do not include it in the analysis, we note that the ghosts

---

[1] http://www.stsci.edu/hst/wfc3/ins_performance/anomalies .

[2] In the Ball Aerospace System Engineering Report of Turner-Valle (2000), the angles of incidence of the front surfaces of each of the windows and the surface of the detector are given as 0.9835 degrees and 20.90719 degrees, respectively. The difference is 19.9237 degrees.

[3] For the Advanced Camera for Surveys (ACS), Woodruff and Cahill (1998) list the window-CCD tilt angles as 20.2° (ACS WFC) and 30.8º (ACS HRC).

will be (strongly) linearly polarized, even for unpolarized sources, due to the large angles of incidence of the light to the surfaces of the windows and detector.

Ghosts of Stars

In order to derive the locations of the ghosts, we let D_{sc} be the projection upon the diagonal of the vector from the star to the lower-right corner of quadrant D (Figure 3). Then, neglecting optical distortion, the separation of a star and its ghost is

$$d_i \approx 2 (D_{sc} \sin\theta + b_{0,i}) \sin2\theta / \cos3\theta ,$$

where $b_{0,i}$ is the minimum separation between the detector (at its corner) and the ith window surface (θ and b are indicated in Figure 2). We cannot measure $b_{0,i}$ directly, but we can recast the equation above in terms of θ and quantities that we can measure on the detector:

$$d_i \approx 2 D_{sc} \sin\theta \sin2\theta / \cos3\theta + d_{0,i} ,$$

$$d_i \approx 0.941 D_{sc} + d_{0,i} , \text{ for } \theta = 20.375° ,$$

where the minimum ghost-star separation, i.e. for a star in the corner where $D_{sc} = 0$, is $d_{0,i} = 1376, 1611, 4020,$ and 4816 pixels, for ghosts $i = 1, 2, 3,$ and 4 respectively.

The ghosts are elliptically shaped annuli, with the ratio of semimajor to semiminor axes, the ellipticity $\approx 1/\cos 3\theta \approx 2.0$. The ratio of the distance (d) from a star to its ghost and the semimajor axis (a) of the ghost's ellipse, $d/a \approx 20$. The latter ratio, and the ellipticity are both scale-invariant and hence are the same value for all window ghosts, aside from very small differences associated with optical distortion. To a good approximation, a ghost's semimajor axis

$$a_i \approx 0.047 D_{sc} + a_{0,i} ,$$

with $a_{0,i} = 68, 79, 198,$ and 238 pixels for ghosts $i = 1, 2, 3,$ and 4 respectively. The area[4] of each elliptical ghost is $\pi a_i^2 / 2.0$, where again 2.0 is the ellipticity, which respectively equal $6800, 9300, 58000,$ and 83000 pixels for $i = 1, 2, 3,$ and 4, and $D_{sc} = 0$, i.e. the minimum area of each ghost. Table 1 lists properties of ghosts for six representative locations of a star in quadrant D.

---

[4] Due to obscuration of the primary mirror, the area of each annular ellipse is ~20% less that which we report for the entire ellipse, due to the central obscuration (Burrows et al. 1991).

The properties of the ghosts described above and in Table 1 are have been calibrated to the observed ghosts at 633 nm. Because the WFC3 UVIS system is a well-designed optical system, chromatic shifts of the primary images should be negligible for our purposes, and because the 1st ghost is formed by three reflections and no refraction, the position of the 1st ghost should also be achromatic. However, there should be very slight shifts in the positions of the 2nd, 3rd, and 4th ghosts with wavelength, due to the refraction at the window surfaces. Using Snell's law and an angle of incidence of ~40 degrees on a plane-parallel plate of fused silica glass, and for refractive indices ranging from 1.45 (633 nm) to 1.50 (~250 nm), we estimate that the separation between the 1st ghost and the 2nd ghost will be ~4% less at 250 nm than at 633 nm, which amounts to less than 13% of the semimajor axis of the smaller ghost's ellipse. Although this analysis predicts that the positions of the edges of the flare that appears in flat fields (described in the next section) are very slightly wavelength dependent, we expect the wavelength dependence will be too small to be measurable in flat fields, primarily because the shift is a small fraction of the width of the defocused edges of the flare.

We measured the properties of the ghosts from a thermal vacuum test, "UV26S13 glint map part3," of many images, each on-chip binned 3x3, of a HeNe laser spot (633 nm) focused upon the UVIS detector through filter F625W in a grid of positions (Brown 2008). In the test, executed from 2008-03-31 21:01 to 2008-04-01 4:36, the first exposure was 1 second, and the others were each 25 seconds. In the 36 longer exposures we analyzed, the laser spots are organized in a 6x6 regular grid across quadrant D. The longer exposures saturate the laser spots but give good sensitivity to the defocused ghosts, and the 1-s exposure provides an unsaturated laser spot to calibrate the others. Aperture photometry (circular, r=5 pixels) of the unsaturated laser spot at $(X,Y) =$ (679,625) gives 133407 DN in a 1-sec exposure of a HeNe laser (@632.8 nm) attenuated 86 dB.

In order to visualize the ghosts, in Figures 4 and 5, we co-added the images that contained ghosts into one single image, while clipping the noisy, nearly zero-level pixels to zero in each image to avoid co-adding noise and thereby reducing sensitivity to the ghosts. We used the co-added image to make the figures in this document and to measure the locations of the ghosts and their shapes, but to measure the ghosts' brightnesses, we used a single image, the one in which the saturated laser spot appears closest to the lower right corner.

For the photometric analysis, we median filtered that single image with a 5x5 pixel kernel to eliminate cosmic rays. We then summed the counts in each of the four elliptical ghosts of the saturated laser spot in the lower right corner. The largest-diameter ghost has ~4 DN/pixel surface brightness.[5] In order to evaluate the effect of background subtraction, we subtracted either of two representative backgrounds, one below or one to

---

[5] Due to the 3x3 binning, this corresponds to ~0.4 DN/pixel for the native CCD pixels.

the right of each elliptically shaped ghost. The background measurements ranged from 0.53 DN/pixel to 0.90 DN e/pixel, corresponding to 13% to 22% of the surface brightness of the faintest ghost, which as mentioned before is ~4 DN/pixel. The resulting fluxes from the four ghosts (ordered from nearest to farthest from the laser spot) are 24549, 23088, 24523, and 21929 DN, each with an estimated 1-sigma uncertainty of 800 DN. The latter was estimated to equal the maximum of the absolute value of the differences between the two measurements of the background associated with each ghost. From those measurements and the measurement of the unsaturated laser spot, we estimate the four ghosts (in the same order as before) are 0.74%, 0.69%, 0.74%, and 0.66% of the primary image's flux. The 1-sigma uncertainty of each due to the ghost photometry is 0.024%; however, the uncertainty due to the laser spot photometry is considerably more as we discuss in the next paragraph.

Scaling from the unsaturated laser spot's photometry, we predict 3.33M DN in the saturated spots that had 25 times longer exposures. However, our attempt at validating that estimate produced confusing results. The 3x3 on-chip binning caused the spots' saturation to a) bleed in the horizontal serial registers, and b) saturate the ADC, producing zeros in the "*raw.fits" images at centers of the PSFs (see Figure 1 of Brown 2008). For the 6x6 grid of stars, using a 25 pixel by 25 pixel aperture to include nearly all of the spot's wings and bleed trail, and ignoring for the moment the ADC saturation, we measured the following values, in 1E6 DN:

	C1	C2	C3	C4	C5	C6
R1	0.26	1.56	3.61	3.87	3.82	3.93
R2	1.05	2.37	2.31	2.28	2.27	2.34
R3	0.92	2.28	2.27	2.24	2.38	2.30
R4	1.14	2.28	2.24	2.18	2.27	2.29
R5	1.33	2.24	2.26	2.23	2.24	2.30
R6	1.30	2.35	2.25	2.29	2.16	2.27

The values in column C1 are low because the spots are on the border of quadrants C and D; in that case, even if the charge was conserved during saturation of the serial register, some of it is lost because the two horizontal bleed trails are truncated (and insidiously not apparent in the "flt.fits" images, but they do appear in the overscan available in the "raw.fits" images).[6] The values in row R1 are affected by the gap between the CCDs: in (only) row R1, this clearly affects the values in columns C1 and C2 and to a lesser degree C3. The values not in C1 nor in R1 (i.e. those fully within quadrant D) all equal 2.3 within 6%, which suggests that the laser spot is not variable, which otherwise might have been a concern due to mechanical shifts affecting optical coupling of the laser light to the instrument. While the measured spot flux of 2.3 M DN is 0.69 times the predicted flux of 3.33 M DN, we could rationalize that as due to the ADC-saturated pixels' charge not being measured. On the other hand, the measurement at

---

[6] The unsaturated star's center is 4 binned pixels (12 native pixels) from the quadrant boundary.

(R1,C6) is 3.93, or 18% more than the prediction of 3.33, which cannot be rationalized so easily. It isn't that the unsaturated star is clipped by the quadrant boundary like the other stars in C1: it is 4 binned pixels (12 native pixels) from the quadrant boundary so only an insignificant fraction of its wings extend across the quadrant boundary and anyway are recorded accurately by the CCD's other amplifier.

Notwithstanding concerns for the accuracy of the photometry, our ghost-to-primary-image measurements are ~0.1% smaller than those predicted by Stiavelli (2001) also @ 632.8 nm, based upon ray tracing and a ~30% reflectivity from the detector and ~2.4% reflections from each window surface: 0.860%, 0.812%, 0.767%, and 0.725%. Note that in Stiavelli's prediction, each of the latter ghosts is fainter than the previous one by the factor 0.945.[7]

Combining our measurements with Stiavelli's analysis, we recommend adopting[8] at 633 nm a window interface reflectance r=0.025, a detector reflectance of 0.30, and thus the following fraction of light for the nth ghost to the primary image: $0.3*r*(1-r)^{2(n-1)}$, i.e. 0.750%, 0.713%, 0.678%, and 0.644%. Each of the latter ghosts is fainter than the previous one by the factor 0.95. The total of all four ghosts is 2.78% and is consistent with a prior estimate of approximately 3% through F814W (Brown & Lupie 2004).

In order to determine the wavelength dependence of the ghosts, we measured the ratio of each ghost's surface brightness to that of the star on six images of a star cluster from program 11911. One very bright, blue, and saturated star produces a detectable ghost with a semimajor axis ~100 pixels in filters F225W, F275W, and F336W. Another one, a very bright, very red, and saturated star produces a detectable ghost with semimajor axis ~120 pixels in filters F775W, F814W, and F850LP. In each case, the ghost is very difficult to measure amongst the crowded star field. Our measurements, normalized to a what a ghost of surface area 6800 pixels would produce, yield ghost-to-star ratios of 2.9, 3.9, 3.8, 3.3, 2.8, and 3.1 ppm in filters F225W, F275W, F336W, F775W, F814W, and F850LP, respectively. Those may be compared directly to our estimate of 6.1 ppm for 633 nm measured using the HeNe laser spot, described in the next paragraph. Apparently our measurements from the crowded star cluster are ~2x smaller than those using the HeNe spot. We have no explanation for the disagreement other than the analysis of both observations are challenging due to the large dynamic range required, and that neither test was designed specifically to measure photometrically the ratio of ghost to primary image. In this report we adopt the HeNe laser spot value (derived below) for the photometric

---

[7] The ~2.4% reflectance at 633 nm, plotted in Stiavelli's Figure 5 is not estimated for the ~40 degree angle of incidence of the ghost light upon the window surfaces; also, Stiavelli (private communication) recalls that the example coating design in his Figure 5 was not the one selected for the flight model of WFC3. The 0.945 decrement factor, from one ghost to the next, would be commensurate with a 2.8% reflectance, i.e. 1-sqrt(0.945).

[8] We adopt the detector reflectance of 0.30 and then choose r=0.025 so that the predicted four ghost-to-primary fractions approximate those we measured.

ratio at 633 nm, and consider the star cluster measurements as evidence for an approximately flat response with respect to wavelength. In the Appendix, we analyze the wavelength dependence, including polarization for the glancing incidence reflections, but not including anti-reflection coatings; results are in Table A1.

The minimum area of any ghost is ~6800 pixels, and the maximum surface brightness S in a ghost from a star with a (predicted[9]) spatially-integrated detected flux F (e s^{-1}) is

$$S = 0.0075 \ F \ / \ 6800 = \sim 1.1E\text{-}6 \ F \ (\text{e s}^{-1} \ \text{pix}^{-1}),$$

in which we have used the largest ratio, 0.75%, of the ghost flux to primary image flux, based upon measurements at 633 nm. Because the peak pixel's ensquared energy[10] is ~0.18 F, the maximum ratio of surface brightness in the window ghost to that of the peak-pixel (DN s^{-1} pixel^{-1}) of the star is ~6.1 ppm, or 13 astronomical magnitudes. Because the largest of the 1st or 2nd ghosts have areas of ~40,000 pixels, we expect that the largest of those ghosts will have surface brightness ratios of ~1 ppm or 15 mag. From Table 1, the very largest, but much more rare 3rd and 4th ghosts will be twice as large as that, i.e. ~80,000 pixels, and hence ~0.5 ppm (15.8 mag) fainter than the peak of the responsible star. Using the exposure time calculator, we estimate that in F606W, a V=15.0 solar-type star located at the lower-right corner of quadrant D, i.e. located so as to maximize the visibility of its window ghosts, will produce ghosts 1, 2, 3, and 4 that are 62%, 43%, 6%, and 4% as bright as the sky with average zodiacal and earthshine contributions. If we define 10% of average sky as a threshold below which a ghost may be considered unimportant, then stars fainter than V=17 produce only unimportant window ghosts in F606W. Table 2 provides comparable threshold values for a grid of positions of the star in quadrant D; it also confirms the locations that can produce these ghosts illustrated in Figure 4 of Brown (2007). As a similar benchmark for narrowband imaging, in which the CCD read noise (3 electron r.m.s.) tends to be more important than sky noise, we estimate that the brightest ghost that a V=14 mag star imaged in F656N can produce in a 1000-s exposure is 0.5 e pixel^{-1}, which is marginally detectable over the (minimum) area of 6800 pixels.[11] Scaling from Table 2, we predict that, more typically in quadrant D, a star will need to be brighter than V~12 to exhibit these ghosts in narrowband images.

---

[9] We emphasize "predicted" flux because if the ghost is detectable, the star will be saturated and its measured flux may be underestimated.
[10] WFC3 Instrument handbook, Table 6.9 lists ensquared energies; here we use the value for 600 nm.

[11] Formally it's 13-sigma, but still only marginally detectable in simulated images.

Stiavelli et al. (2001) predicted that individual ghosts would become visible at the 4 e/pixel level in full orbit[12] F606W exposures for stars in the magnitude range 15.7 to 14.6. They also predicted that individual detector-window ghosts would have relative intensity per pixel in the range 0.15 ppm to 0.075 ppm. Our analysis supports a rule of thumb that V=15 stars produce marginally detectable ghosts (see Table 2). Inexplicably, their prediction of "4 e/pixel" is ~4 times smaller than our ETC estimate of 15 e/pixel for ghosts 10% as bright as an average sky in a 45-min F606W exposure produced by stars (cf. Table 2) in the range discussed by Stiavelli et al. (V mag from 15.7 to 14.6). Also, their prediction of "0.15 ppm" is smaller than our estimate of the peak surface brightness by a factor of 40 and their dynamic range of "0.15 ppm to 0.075 ppm" is only a factor of two, whereas we have calculated that the ghosts' surface areas have a dynamic range of ~13 (Table 1). Stiavelli et al.'s smaller dynamic range may have originated from their Table 2, in which they list the "radius" of each of the four detector-window ghosts as 2.1, 2.2, 2.8, and 3.2 mm, whereas we have shown that the minimum lengths of the ghosts' semimajor axes are $a_{0,i}$ = 1.0, 1.2, 3.0, and 3.6 mm, for a pixel size of 0.015 mm. We find that Stiavelli et al.'s "radii" match well ghosts' semimajor axes selected from the center of quadrant A: to make the comparison, based upon Figures 6-9 we selected ghosts corresponding respectively to the 4th, 4th, 1st, and 1st rows of each of the sections of Table 2, specifically semimajor axes a = 151, 163, 203, and 243 pixels, or 2.3, 2.4, 3.0, and 3.6 mm, which are approximately 10% larger than Stiavelli et al.'s values.

Ghosts of Flat Fields

We numerically simulated the summation of the many defocused ellipses from a uniform illumination of the detector. The result (Figure 3) replicates the wedge-shaped flare apparent in flat fields (Figure 10) in many respects: the locations of the vertices of the four wedges, the opening angle of the wedges, and (very) approximately the surface brightness of each wedge (through filter F606W).

It is useful to note that the four discrete surface brightnesses of the interiors of the wedges are approximately one half the ghost reflection (flux) fractions recommended in the previous section, because whereas surface brightness is conserved along rays, the projection of the flat field's ghost upon the tilted detector dilutes each ghost's surface brightness by the ratios of the direction cosines of the rays incident upon the detector as ghosts and as direct images, i.e. by the factor $\cos(3\theta) / \cos\theta$, or ~0.515 for θ = 20.375°. In our numerical simulations, each of the discrete ghosts covers 41%, 37%, 7%, and 2.7% of the combined area of the two CCDs, and the associated surface brightness dilution of each (which we expected analytically to be 0.515) is 0.506, 0.513, 0.510, and 0.496. The latter measurements are the medians of the non-zero values of the simulated images of

---

[12] We interpret "full orbit" as 45 minutes, not the 96 minute period of HST, due to Earth occultation for approximately half the orbit.

each ghost, so we attribute the somewhat smaller value (0.496) associated with the 4th ghost is simply due to the larger fraction of pixels near the wedge's edge (pulling down the median slightly) compared to its "plateau" value which the analytic value predicts. Combining the analytic surface brightness dilution factor of 0.515 with the flux ratio of 0.75% for the 1st ghost and the decrement of 0.95 for each successive ghost (due to reflective losses at the window surfaces), we predict the surface brightness contributions of the four wedge-shaped features to be 0.386%, 0.367%, 0.349%, and 0.331% of the flat field's surface brightness, or cumulatively, 0.386%, 0.753%, 1.102%, and 1.433%.

Also, one can show that the opening angle Ω at the vertex[13] of the wedge-like feature on the detector is $2 \tan^{-1}(1 / (1 + \partial d / \partial D_{sc})) = 54.5°$. Slight changes in θ about its nominal value of 20.375° would result in ~4 times that change in Ω in the opposite direction; e.g. $\theta = 20.5° \rightarrow \Omega = 54.0°$ and $\theta = 20.25° \rightarrow \Omega = 55.0°$.

The wedge's vertex in observe flat fields is not precisely where predicted. The cause appears to be that the reflective silicon of the CCD extends slightly beyond the active area that is read out as pixels, and our simulation did not account for the outer "rind" of reflectivity. As long as the reflective area has a square shape, the shape of the wedge-shaped flare will be the same, just shifted a bit along the diagonal (closer to the quadrant D's corner). We have found other evidence that the reflective area extends beyond the active CCD pixels. In image IBE401DLQ of program 12077, a star (R=14 mag) has drifted ~0.8 arcsec off the lower edge of the CCD and yet still produces a ghost. In image IBE401DJQ, taken at nearly the same moment, the same star has drifted ~1.0 arcsec off the lower edge and produces no detectable ghost. This implies that the area of the focal plane that produces ghost reflections extends ~0.8 arcsec (~20 pixels) beyond the lower edge of the active imaging pixels of the CCD. Similarly, in image IBC601H2Q of program 11924, the star GSC2 N2JQ022863, a V=16.18 star 1.5 arcsec off the right edge near the lower-right corner, casts a well-detected ghost. However, in the same image, N2JQ142792 is a V=15.28 star 1.7 arcsec off the right edge and even nearer to the corner, but its ghost is fainter than the aforementioned one, suggesting its ghost is attenuated by vignetting at the edge (or the corner). These examples suggest that the effective edge of the reflective area of the focal plane may not be predictable precisely. A practical solution may be to shift the model until it best matches the wedge-shaped feature in an observed flat field.

---

[13] Because the wedge-shaped flare results from the superposition of innumerable elliptical ghosts, the vertex is not a sharply defined point. In our discussion of the opening angle, we are referring to the angle between the two lines defined by the <u>centers</u> of the elliptical ghosts generated by reflections at the edges of the silicon detector.

Discussion

Returning for a moment to the design of WFC3 UVIS, we see that to prevent detector-window ghosts from landing on the detector, the minimum detector-to-window separation b must be larger than 0.5 cos 3θ / sin 2θ times the length of the detector's diagonal, in order that the ray incident upon the lower right corner of the focal plane will produce a ghost that lands at or beyond the far corner. For θ = 20.375°, the factor 0.5 cos 3θ / sin 2θ equals 0.375. If the inner-most window surface was slightly further from the detector than the actual position of the outer-most window surface, then from Figure 4 we note that the 1st ghosts would land further to the upper left along the diagonal than the 4th ghosts actually do, and in that case, the design would have prevented all of these ghosts from landing on the detector entirely.

The individual stellar ghosts typically are only a nuisance for scientific observations, because only relatively bright stars located in a relatively small area of the focal plane can create detectable ghosts, much less have those ghosts also, per chance, overlap targets of scientific interest. However, the ghosts of the flat fields are a significant calibration issue that should be and is being addressed. The ghosts add ~1% extra light over ~40% of the focal plane in observations of flat fields, or large, diffuse astronomical objects such as nearby galaxies, or the sky itself. If one naively calibrates an image by subtracting a bias and dark and then dividing by the (ghost-contaminated) flat field, the calibrated image's uniform sky will look OK, but the fluxes of stars in the affected ~40% of the focal plane will be underestimated by ~1%. On the other hand, if one were to then simply correct the bias-dark-flattened image using a map of the sensitivity to star-like objects, i.e. apply an L-flat, then the sky's surface brightness would be wrong, because of the instrument's wedge-shaped stray light (ghost) feature. Further discussion of corrections to the calibration of UVIS images is beyond the scope of this report.

Ironically, the same UVIS quadrant A that is affected by the flat-field ghosts is also the quadrant that contains subarray UVIS1-C512A-SUB, the most often selected one for photometric calibration in the period June 2009 to August 2010 (see e.g. Kalarai 2010; cf. his Figure 2 with his Figures 3-5) and the one selected for higher signal-to-noise monitoring of temporal stability (Kalarai's Figure 6). In Cycle 17, quadrants A or B were the ones containing 512x512 subarrays made available to General Observers, whereas in Cycle 19, the 512x512 subarrays available to GOs are from quadrant C (Figure 6.2 of the Cycle 19 WFC3 IHB). The switch away from quadrant A is a good choice in light of the complication of the ghosts' effect on flat fields.

Conclusions

We analyze detector-window ghosts in WFC3 UVIS. Our geometric model predicts the locations, shapes, and brightnesses of the ghosts of stars. Each ghost is elliptically shaped, with an aspect ratio of 2:1, and oriented with its major axis parallel to the

diagonal connecting quadrant A to quadrant D. In filter F606W, the ratio of a window ghost's surface brightness to that of the brightest pixel of the responsible star's PSF ranges from 0.5 ppm for the largest ghosts to 6 ppm for the smallest ghosts. Each V = 15.0 mag star in the lower right corner of the UVIS focal plane (in quadrant D) will produce two ghosts in quadrant D that are ~50% as bright as the sky in F606W, and two ghosts in quadrant A that are ~5% as bright as sky. We created an XML format overlay that may be used with APT and Aladin to predict the locations of ghosts, as described in Appendix B.

The detector-window ghosts also explain a wedge-shaped "flare" visible in flat field images. The wedge actually is the superposition of four components, each with an opening angle equal to 54.5° approximately centered on the UVIS diagonal. At ~600 nm, we estimate the wedge to have four levels of surface brightness equal to 0.386%, 0.753%, 1.102%, and 1.433% of the flat field itself. We make an approximate prediction of the wavelength dependence of the ghosts and a few measurements of the ghost-to-primary-image ratio both of which suggest only a weak wavelength dependence. Including the geometric model of the ghosts in the analysis of "star flats" (a.k.a. "L flats") may improve those flats, because the wedge's edges are sharp and spatially unresolved by the "L flats."

References

Baggett, S. 2005, WFC3 Thermal Vacuum and Ambient Testing: Calibration Subsystem Performance, ISR WFC3-2005-09.

Brown, T. 2007a, UVIS Channel Ghosts after Filter Replacement, ISR WFC3-2007-09.

Brown, T. 2007b, WFC3 TV2 Testing: UVIS Channel Glint, ISR WFC3-2007-21.

Brown, T. 2008, WFC3 TV3 Testing: UVIS Channel Glints, ISR WFC3-2008-07.

Brown, T. & Lupie, O. 2004, Filter Ghosts in the WFC3 UVIS Channel, ISR WFC3-2004-004.

Burrows, C. et al. 1991, ApJ 369, L21.

Bushouse, H. 2005, WFC3 Thermal Vacuum Testing: UVIS Broadband Flat Fields, ISR WFC3-2005-21.

Fineberg, D. 2009, Wide Field Camera 3 Instrument Description and User's Handbook, Final Version, Hubble Space Telescope Library #TM-035454, 442-RPT-00113

Jackson, J. D. 1975, Classical Electrodynamics, 2nd edition, Equations 7.39 and 7.41.

Kalarai, J., Baggett. S., Borders, T., and Rajan, A. 2010, The Photometric Performance of WFC3/UVIS: Temporal Stability Through Year 1, WFC3-ISR-2010-14.

Stiavelli, M., Sullivan, J., and Fleming, J. 2001, Modeling the impact of ghosts on WFC3/UVIS, ISR WFC3-2001-17.

Table 1: Properties of Window Ghosts, from the model. Columns are the star's (X,Y) center, the ghost's (x,y) center, the distance from the star's center to the ghost's center, the ghost's semimajor axis "a" and its area, all in units of native CCD pixels, or pixels squared. The ghosts are enumerated in the same convention used throughout this paper. For compactness of the table, we list only the subset of stars near the CCD's diagonal from the 6x6 matrix of positions illustrated in Figures 6-9. Asterisks indicate that no part of the ghost lands on the CCD.

```
     X         Y        x        y       d       a      Area

Ghost 1 (nearest to star):

4047        99     3019     1152    1471     73      7800
3645       492     2245     1922    2001     99     14400
3246       888     1475     2665    2508    125     23000
2841      1284      696     3441    3041    151     33700
2436      1680      -82     4217    3575    178     46500
2040      2085     -851     5003    4108    204     61300*

Ghost 2:

4047        99     2854     1320    1707     84     10500
3645       492     2080     2060    2215    111     18000
3246       888     1310     2833    2744    137     27500
2841      1284      531     3609    3277    163     39100
2436      1680     -247     4385    3810    189     52800*
2040      2085    -1016     5171    4343    216     68500*

Ghost 3:

4047        99     1168     3010    4094    203     60900
3645       492      394     3780    4623    229     77600
3246       888     -375     4553    5152    256     96200*
2841      1284    -1154     5329    5685    282    117100*
2436      1680    -1933     6104    6218    308    140000*
2040      2085    -2702     6890    6751    335    164900*

Ghost 4:

4047        99      610     3579    4890    243     86800
3645       492     -162     4348    5419    269    106500*
3246       888     -932     5122    5948    295    128200*
2841      1284    -1711     5897    6482    321    152100*
2436      1680    -2491     6673    7015    348    178000*
2040      2085    -3260     7459    7548    374    206000*
```

Table 2: Thresholds for ghosts, from the model. For the 6x6 matrix of stellar positions illustrated in Figures 6-9, we list the V magnitude at which a F606W exposure will produce a ghost with a brightness equal to 10% of an average sky. Asterisks indicate positions at which no part of the ghost lands on the CCD.

```
               Ghost 1 (nearest to star):

                 *     *     *     *    15.3 15.5
                 *    14.9 15.1 15.3 15.5 15.7
                 *    15.1 15.3 15.5 15.7 16.0
                 *    15.3 15.5 15.7 16.0 16.3
               15.3 15.5 15.7 16.0 16.3 16.6
               15.5 15.7 16.0 16.3 16.6 17.0

               Ghost 2:

                 *     *     *     *    15.1 15.3
                 *     *    15.0 15.1 15.3 15.5
                 *    15.0 15.1 15.3 15.5 15.8
                 *    15.1 15.3 15.5 15.8 16.0
               15.1 15.3 15.5 15.8 16.0 16.3
               15.3 15.5 15.8 16.0 16.3 16.7

               Ghost 3:

                 *     *     *     *     *     *
                 *     *     *     *     *     *
                 *     *     *     *     *     *
                 *     *     *     *     *    14.4
                 *     *     *     *    14.4 14.5
                 *     *     *    14.4 14.5 14.7

               Ghost 4:

                 *     *     *     *     *     *
                 *     *     *     *     *     *
                 *     *     *     *     *     *
                 *     *     *     *     *     *
                 *     *     *     *     *    14.2
                 *     *     *     *    14.2 14.3
```

Appendix A: Wavelength Dependence of the Ghosts

Using the Fresnel reflection coefficients for acute angles of incidence upon uncoated optically flat surfaces of fused silica and silicon, we estimate here the ratio of flux in the ghost to that in the primary image from first principles.[14] We use the formulae from Jackson (1975) and the wavelength dependent indices of refraction for fused silica and silicon.[15] The former is purely real and the latter is complex, i.e. includes opacity in the medium, especially in the UV; in Table A1, the real component is "n" and the imaginary component is "k." The results are tabulated in Table A1 and illustrated in Figure 11.

---

[14] Caveat emptor: our calculations neglect anti-reflection coatings on the glass (single-layer MgF_2) and detector (proprietary) and hence should be used with caution.
[15] http://www.filmetrics.com/refractive-index-database/Si/Silicon and http://www.filmetrics.com/refractive-index-database/SiO2/Fused-Silica-Silica-Silicon-Dioxide-Thermal-Oxide-ThermalOxide .

Table A1: Predicted characteristics of reflections. Columns: 1) wavelength, 2) refractive index for fused silica, 3-4) refractive index for silicon (n=real, k=imaginary), 5-7) ghost 1 to primary image flux ratio in % for linear polarized components: perpendicular, mean, and parallel; 8-10) perpendicular polarization reflectances (R1, R2, and R3, each in units of 1E-4) at surface 1 (silicon at θ), surface 2 (fused silica at 2θ), and surface 3 (silicon at 3θ); 11-13) same for mean of perp. and para.; 14-16) same for parallel polarization. The ghost-to-primary ratios in columns 5-7 have all been multiplied by 0.7 in order for the average ratio at 0.633 um to match the observations of a HeNe spot. The ghost-to-primary ratios for ghosts 2, 3, and 4 are successively less than ghost 1's and are only weakly dependent on wavelength because the only difference is the number of reflections from the fused silica. To compute the mth ghost-to-primary ratios, multiply columns 5-7 by $0.7(1\text{-}R2)^{2(m-1)}$.

Wave [um]	n(SiO2)	n(Si)	k(Si)	ghost/primary [%] perp	avg	para	perp [1E-4] R1	R2	R3	mean [1E-4] R1	R2	R3	para [1E-4] R1	R2	R3
0.20	1.5488	0.9813	2.8974	1.18	0.76	0.34	2793	895	5142	2574	529	2798	2356	164	454
0.22	1.5285	1.2252	3.1742	1.26	0.82	0.38	3205	851	5533	2978	501	3103	2751	151	672
0.24	1.5133	1.5833	3.3717	1.32	0.86	0.41	3557	819	5846	3325	480	3368	3094	142	890
0.26	1.5024	1.6834	4.0621	1.46	0.97	0.49	4194	796	6375	3960	465	3866	3727	135	1357
0.28	1.4942	2.9198	5.2859	1.73	1.20	0.67	5341	778	7232	5121	454	4833	4902	130	2433
0.30	1.4878	5.0036	4.1619	1.76	1.23	0.69	5593	765	7407	5379	446	5058	5165	127	2710
0.32	1.4827	5.0234	3.2997	1.67	1.15	0.63	5325	754	7221	5105	439	4818	4885	124	2416
0.34	1.4787	5.2220	3.0117	1.66	1.14	0.62	5335	745	7228	5115	433	4827	4896	122	2427
0.36	1.4753	6.0519	2.9898	1.73	1.20	0.68	5712	738	7489	5501	429	5167	5290	120	2846
0.38	1.4725	6.4693	0.9665	1.69	1.17	0.65	5609	732	7419	5396	425	5073	5182	118	2728
0.40	1.4701	5.5700	0.3870	1.55	1.05	0.55	5069	727	7038	4844	422	4594	4620	117	2151
0.42	1.4681	5.0890	0.2377	1.46	0.98	0.50	4741	723	6797	4511	419	4315	4282	116	1832
0.44	1.4663	4.7873	0.1693	1.40	0.93	0.46	4515	719	6625	4283	417	4127	4051	115	1628
0.46	1.4648	4.5759	0.1310	1.35	0.89	0.43	4345	716	6494	4113	415	3988	3880	114	1482
0.48	1.4635	4.4202	0.0906	1.31	0.86	0.41	4214	713	6391	3981	413	3882	3748	113	1374
0.50	1.4623	4.2975	0.0730	1.28	0.84	0.39	4107	711	6306	3874	412	3797	3640	113	1288
0.52	1.4613	4.2000	0.0568	1.26	0.82	0.38	4020	708	6235	3786	410	3727	3552	112	1220
0.54	1.4603	4.1197	0.0448	1.23	0.80	0.37	3946	706	6174	3712	409	3669	3479	111	1164
0.56	1.4595	4.0526	0.0326	1.22	0.79	0.36	3883	705	6122	3649	408	3620	3416	111	1117
0.58	1.4587	3.9954	0.0300	1.20	0.77	0.35	3828	703	6077	3595	407	3577	3361	111	1077
0.60	1.4580	3.9473	0.0257	1.18	0.76	0.34	3781	702	6038	3548	406	3541	3315	110	1044
0.62	1.4574	3.9058	0.0220	1.17	0.76	0.34	3741	700	6003	3508	405	3509	3275	110	1015
0.64	1.4568	3.8684	0.0179	1.16	0.75	0.33	3703	699	5972	3471	404	3480	3238	110	989
0.66	1.4563	3.8362	0.0159	1.15	0.74	0.33	3671	698	5944	3439	404	3455	3206	109	967
0.68	1.4558	3.8066	0.0132	1.14	0.73	0.32	3641	697	5919	3409	403	3432	3177	109	946
0.70	1.4553	3.7831	0.0126	1.13	0.73	0.32	3617	696	5898	3385	402	3414	3153	109	930
0.72	1.4549	3.7617	0.0110	1.13	0.72	0.32	3595	695	5879	3363	402	3397	3131	109	915
0.74	1.4544	3.7430	0.0098	1.12	0.72	0.31	3576	694	5862	3344	401	3382	3112	108	902
0.76	1.4540	3.7250	0.0086	1.11	0.71	0.31	3557	693	5846	3326	401	3368	3094	108	890
0.78	1.4537	3.7093	0.0075	1.11	0.71	0.31	3541	692	5832	3309	400	3356	3078	108	879
0.80	1.4533	3.6925	0.0065	1.10	0.70	0.31	3523	692	5817	3292	400	3342	3061	108	868
0.82	1.4530	3.6778	0.0060	1.10	0.70	0.30	3508	691	5803	3277	399	3330	3045	108	858
0.84	1.4527	3.6667	0.0057	1.09	0.70	0.30	3496	690	5793	3265	399	3322	3034	107	850
0.86	1.4523	3.6574	0.0053	1.09	0.69	0.30	3486	689	5784	3255	398	3314	3024	107	844
0.88	1.4520	3.6481	0.0049	1.09	0.69	0.30	3476	689	5776	3245	398	3306	3015	107	837
0.90	1.4518	3.6388	0.0045	1.08	0.69	0.30	3466	688	5767	3236	398	3299	3005	107	831
0.92	1.4515	3.6294	0.0041	1.08	0.69	0.29	3456	688	5758	3226	397	3291	2995	107	825
0.94	1.4512	3.6201	0.0037	1.08	0.68	0.29	3446	687	5749	3216	397	3284	2985	107	818
0.96	1.4509	3.6108	0.0033	1.07	0.68	0.29	3436	687	5740	3206	397	3276	2975	106	812
0.98	1.4507	3.6014	0.0029	1.07	0.68	0.29	3426	686	5732	3196	396	3269	2966	106	806
1.00	1.4504	3.5921	0.0025	1.07	0.68	0.29	3416	685	5723	3186	396	3261	2956	106	799

Appendix B: Using the ghost overlay in APT and Aladin

We constructed an XML format overlay that can be used in APT and Aladin to predict the locations of window ghosts. The overlay, illustrated in Figures 6-7, implements the geometry described in this report for a 6x6 grid of stellar positions in quadrant D. By visual 2-D interpolation of the grid of circles and their associated elliptical ghosts, one can identify which ghosts are associated with which stars in the image. Alternatively, an observer can use the window-ghost overlay in Aladin and STScI's APT to plan observations so as to avoid ghosts interfering with their scientific targets. The latter is described here. For experienced users of APT and Aladin, you may only need the underlined text below.

The first step is to obtain the overlay's XML file. We call it "aladin_WFC3_overlay.xml" but it may be named something else when distributed at WFC3's website or if it is distributed with APT. Next, load a phase 2 file into APT. For this example, illustrated in Figure 6, we retrieved from STScI with APT version 18.4, the phase 2 file for program 11723 (Robert Fesen, P.I.). We selected (clicked on) in turn, Visits, Visit 02, Pattern 1 Exps 3-6, Central SDSS I (0.2.006), Sub Exposures, Central SDSS I (02.006) Pattern 1. We then clicked on "View in Aladin" at the toolbar near the top. An Aladin window opens, showing the two parallelograms representing the WFC3 CCDs. Back in the APT window, we clicked on the "FoV" icon, which then loads the HST focal plane with the other instrument's outlines also. The advantage of selecting the "FoV" within APT is that then APT communicates the orient angle (if defined in the phase 2 file within APT) to Aladin. In the Aladin window, we click on the file folder icon at the upper left. Another window opens offering to look up Aladin images around 02 05 41.5 +64 49 12.2. We could have done that, but in this example, instead we use the "File" icon at the top of that window to browse our local disk for the FITS image that we had previously downloaded from the Hubble Legacy Archive (IB3102060, a 650-second exposure through filter F775W). Even without us clicking on "**SUBMIT**" the image loads in the first Aladin window. It should look like Figure 6, but without the overlay, and probably with not as hard a stretch on the grey scale (to adjust that, click on the "Pixel" icon). To force the grey-scale image to appear underneath the overlays (not on top of them), i.e. to reorder the panes, click on the grey scale image's pane (identified by a galaxy icon next to the filename listed far below the eyeball icon in the upper right corner of the Aladin window) and drag it to the bottom of the list. Then, back <u>in the "Server Selector" window of Aladin, click on "FOV" and then "Load it…" then browse your local disk for the "aladin_WFC3_overlay.xml" file, and choose it. It will appear on Aladin's list, with description "Window Ghosts" of Instrument = "WFC3" and Telescope = "HST." After you **SUBMIT** it, the overlay will appear on the HLA image. Now you need to align those.</u> To do so, choose from Aladin's Zoom pull down menu something small enough that you can see all the FOVs of the instruments of the HST focal plane, in this specific case, probably 1/32x. Aim the cursor at some features of the ghost overlay until a circular arrow appears, then click and you can adjust the rotation angle of that overlay until it matches the HST FOV overlay for Visit 02 - you can use the outlines of STIS and NICMOS as illustrated in Figure 8. Zoom back in, say to 1/4x, and pan as necessary until you have something similar to Figure 6. You may need to fine position the ghost overlay over the image: to do that, aim at the features in the overlay until a hand icon appears, then click and drag. The Ghost overlay and the WFC3 outline in the HST FOVs overlay are not exactly the same but they are close enough for these purposes. When you get Aladin to look similar to Figure 6, then you can use the overlay's circles and ellipses to interpret where the

stars' ghosts will appear by visual 2-D interpolation of the grid of stars and the intermingled four grids of ghosts. To perform the 2-D interpolation, one needs first to study Figures 4 and 5 to understand the patterns of stars and their associated ghosts.
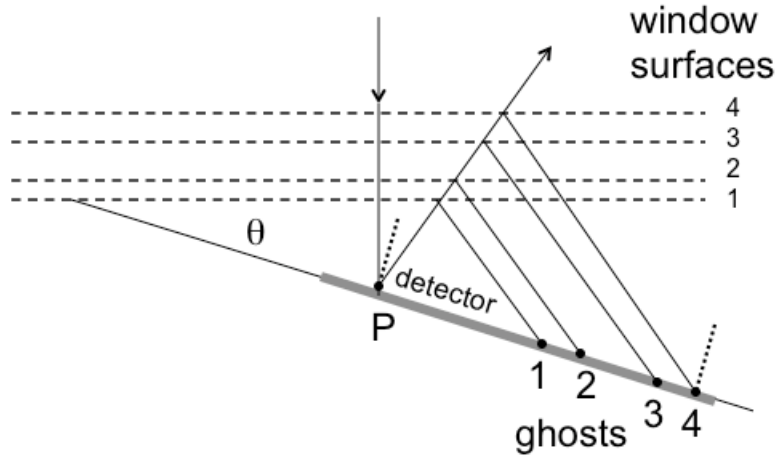
Figure 1: Multiple ghosts. The four surfaces, numbered, of the two panes of glass over the detector (grey) produce four (first-order) ghosts, also numbered, on the detector. The angle of incidence of the ray upon the detector at point P equals the tilt angle θ of the detector relative to the window; the angle of incidence upon the glass surface (vacuum to glass transition) is 2θ, and the angle of incidence of the ray upon the detector at any of the ghosts is 3θ.
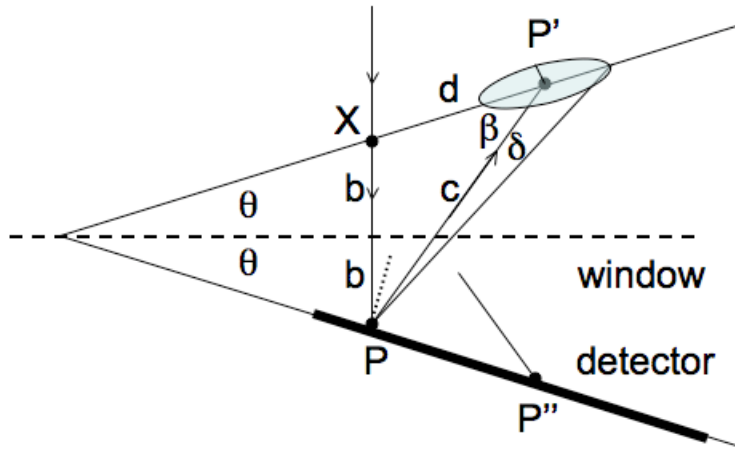
Figure 2: Geometry of ghosts. (Diagram is not to scale). The detector is indicated by the thicker solid line sloping down from the horizontal at angle θ, ~20º. One surface of the window is indicated by the dashed horizontal line (other surfaces are not shown). The thin solid line sloping upward at angle θ is a virtual image plane for the purpose of simplifying the diagram and the analysis. A ray of light, incident from above and having passed through point X, is reflected at point P from the detector. The ray has a ghost reflection from the window and lands on the detector at point P'', which we also indicate in the virtual plane at point P'. The f/31 incident beam expands with angle delta to form a defocused ellipsis shown centered on P'; the same pattern will appear on the detector at P''. The triangle XPP' has sides of lengths 2b, c, and d. The dotted line segment ending at P is normal to the detector; the interior angle XPP' (at point P) is 2θ, hence $\beta = 90º - 3\theta$. Additional formulae are derived in the text.
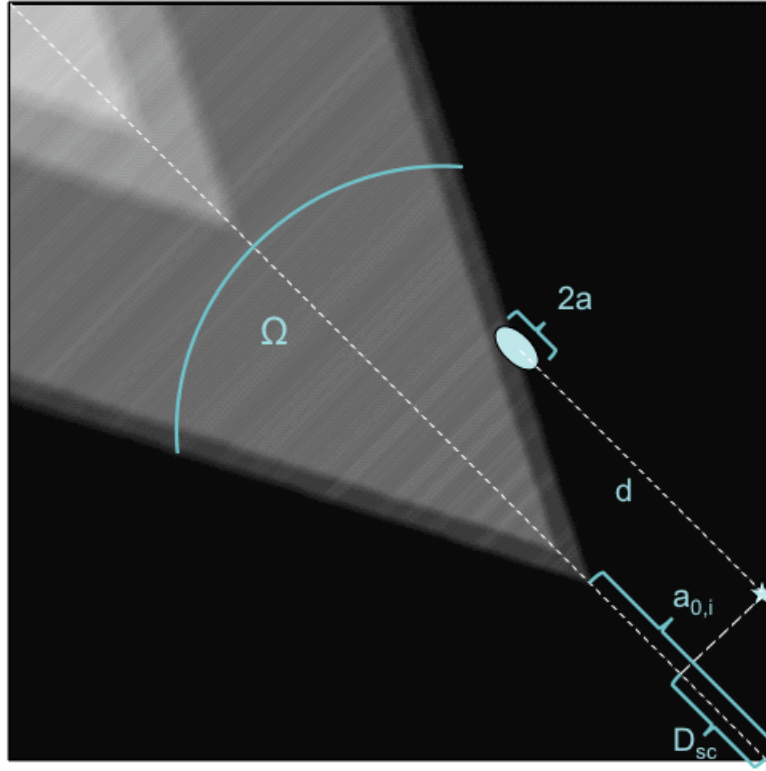
Figure 3: Numerical model (grey scale) of the surface brightness of the ghost components on the UVIS detector. The model is generated by projecting the four defocused ellipses created by the four interfaces of the two glass windows of the chamber. The four ghosts from each point on the detector are mapped according to the geometry in Figure 1; each of the four ghosts has a different value of b, but otherwise the geometric model is identical. The four brightness levels correspond to the superposition of 1, 2, 3, or 4 defocused ellipses. The edges of each wedge are sharper, the closer they are to the wedge's vertex, according to the size of a point-source's defocused ellipse at each location. The opening angle of each wedge at its vertex $\Omega = 54.5°$ (see text). Other parameters from equations in the text are labeled; for $a_{0,i}$ as illustrated, i=1. The diagram is to scale, except for the ellipse. The striation is a numerical artifact and should be ignored.
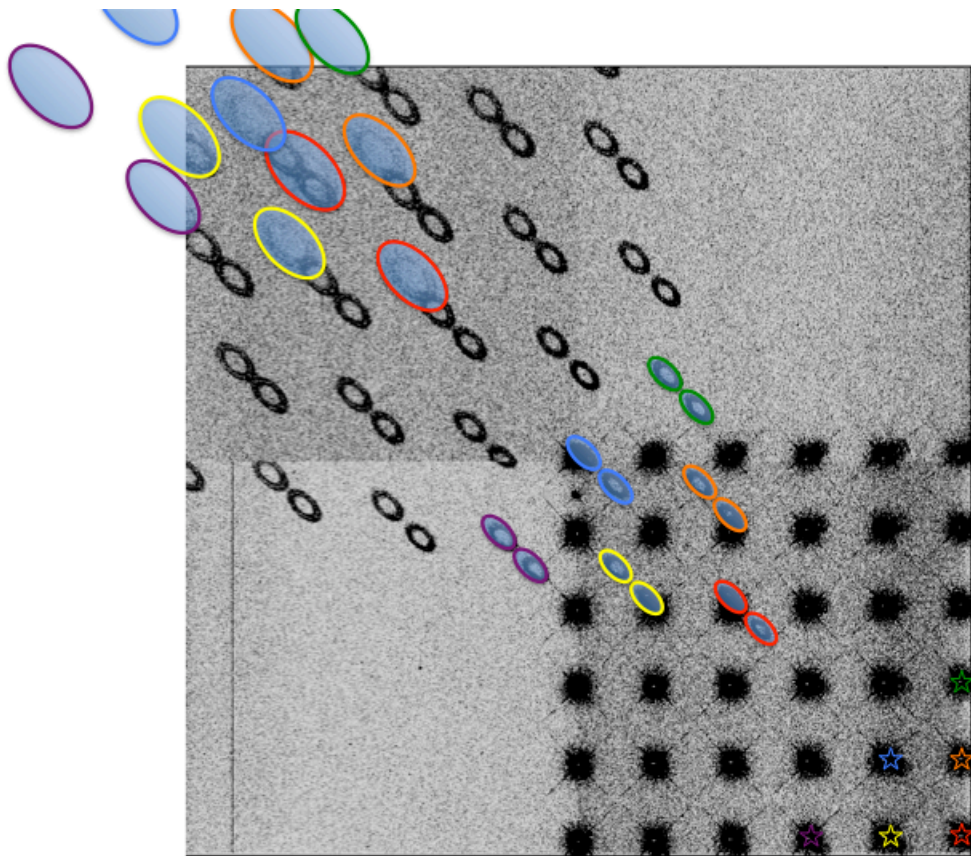
Figure 4: Schematic diagram of ghosts. This figure is a co-added image of 37 individual frames obtained during ground testing in TV3. Each star in the lower right quadrant produces four elliptically-shaped ghosts to the upper left. To aid in identification of the four ghosts associated with each star, we have color-coded six stars and their associated ghosts. Note that of the 36 over-exposed stars in the lower right quadrant, only the one nearest the lower right corner (red) produces four ghosts that land entirely on the CCD.
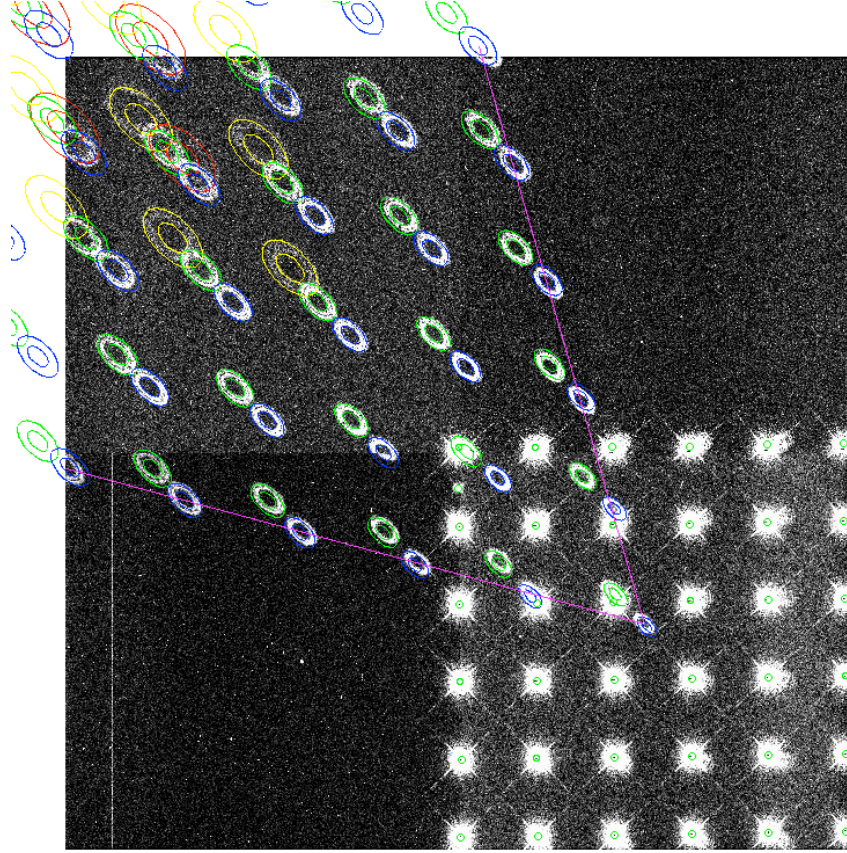
Figure 5: Validation of the geometric model. This diagram overlays the ellipses (colored) as predicted from our geometric model with their observed locations (grey scale image) for the 6x6 matrix of over-exposed stars in the lower right quadrant. The 1st, 2nd, 3rd, and 4th ghosts are colored blue, green, yellow, and red, respectively. The largest relative displacement between the observed ghosts and their respective models is ~half the semi-major axis of the ghost. Green circles identify the centers of the stars; there is a 6x6 matrix of saturated stars and one unsaturated star (immediately below the center of the CCD). The straight magenta lines approximate the border of the wedge-shaped feature apparent in flat fields. In fact, there are four wedge-shaped features: one corresponding to the blue ellipses, a second one corresponding to the green ellipses, a third (yellow ellipses), and a fourth (red ellipses). There is a discontinuity along the horizontal in the middle of the image that is caused by the gap between the two CCDs; the model accounts for the 31-pixel gap.
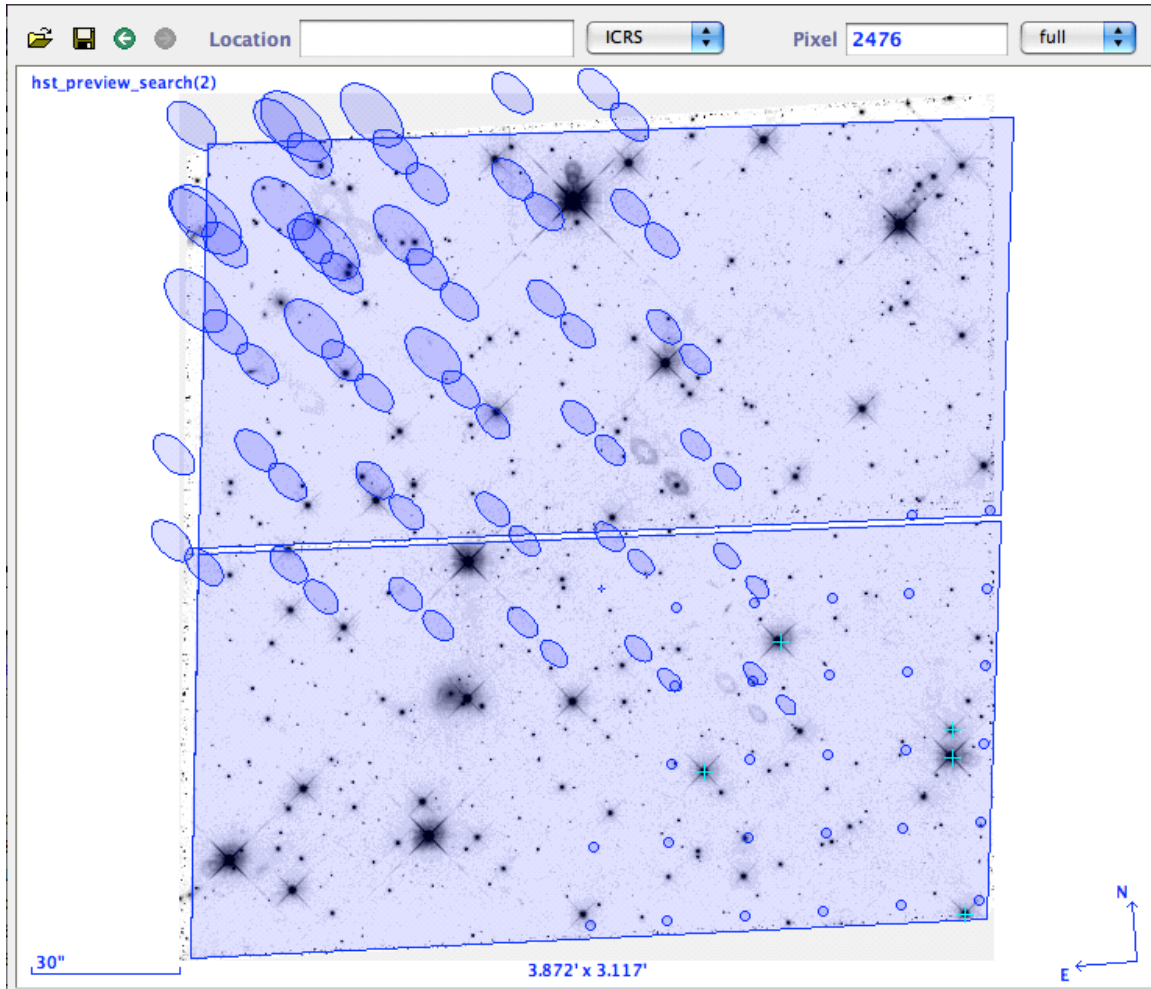
Figure 6: Example of overlay use in Aladin. We obtained the WFC3 UVIS image, named IB3102060 of program 11723 (Robert Fesen, P.I.), from the Hubble Legacy Archive; it's a 650-second exposure through filter F775W of a field near 3C58. Five stars in the lower right quadrant are marked with + symbols. Clockwise from the star in the far lower right corner, the stars' N-band (0.8 micron) magnitudes are 15.59, 14.98, 14.60, ~17, and 13.59. The latter star (N = 13.59 mag) produces the two prominent figure-8 ghosts above the image's center.
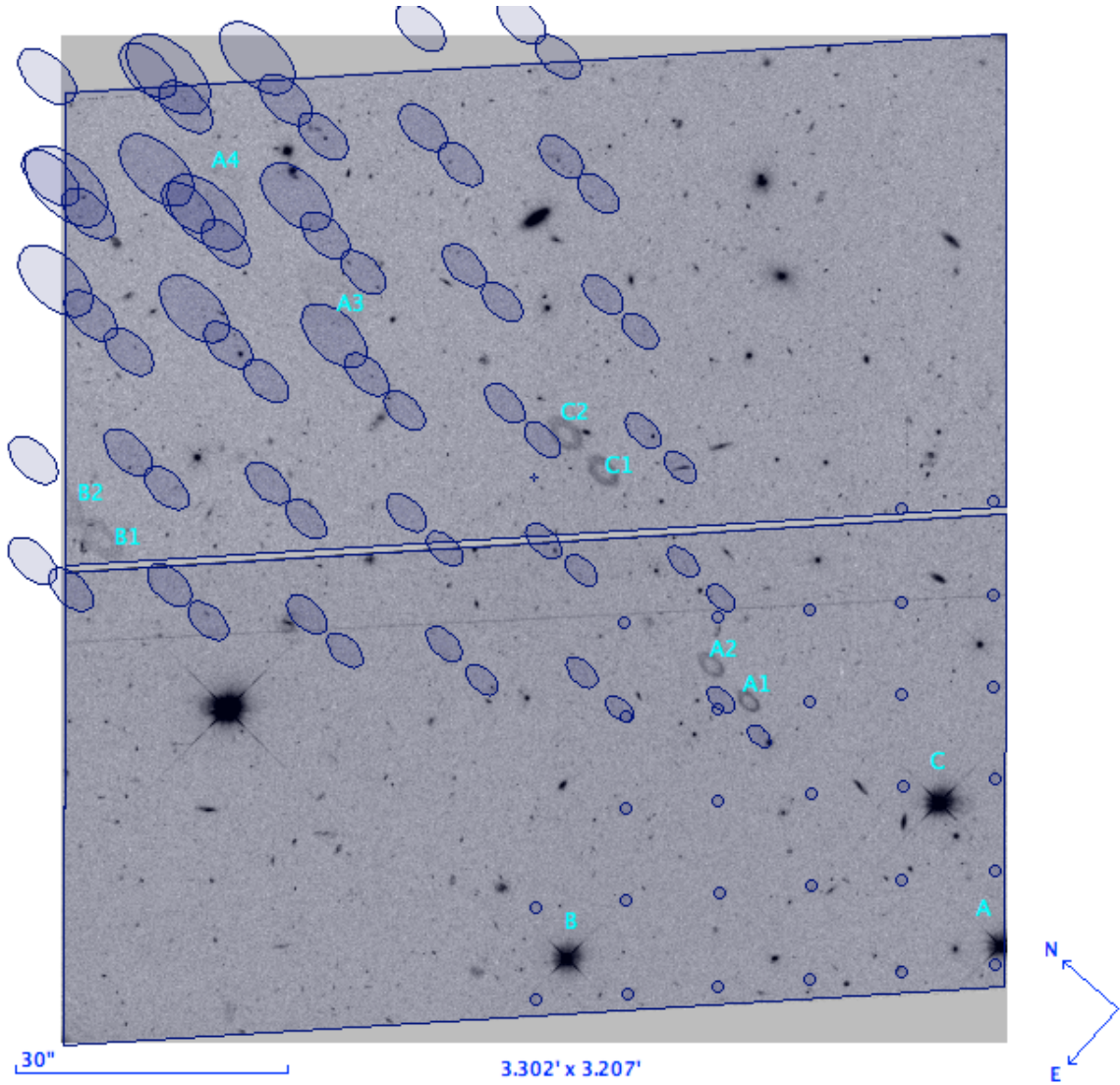
Figure 7: Example of overlay use in Aladin. The model (dark blue overlay) presents an incompletely-filled 6x6 array of circles in the lower right quadrant representing potential positions of stars. (Only positions capable of producing at least one ghost are indicated). By visual 2-D interpolation of the grid of circles and their associated elliptical ghosts, one can identify which ghosts are associated with which stars in the real image. Alternatively, an observer can use the window-ghost overlay in Aladin and STScI's APT to plan observations so as to avoid ghosts interfering with their scientific targets. All four surfaces of the two windows are producing detectable (four) ghosts of the star A in the lower right corner; the ghosts are labeled A1, A2, A3, and A4. The largest ghost, A4, is barely visible above the background. Two pairs of ghosts from stars B and C are labeled and look like rotated figure 8's. Ghost B2 is cut in half by the CCD's edge. We obtained the non-proprietary image, named IB8D73011, from the Hubble Legacy Archive; it's a 2028-second exposure through filter F606W of WFC3 UVIS, taken under program 11700 (Michele Trenti, P.I.). The GSC2.3 V-band magnitudes of the stars A, B, and C are 16.64, 16.49, and 16.07, respectively.
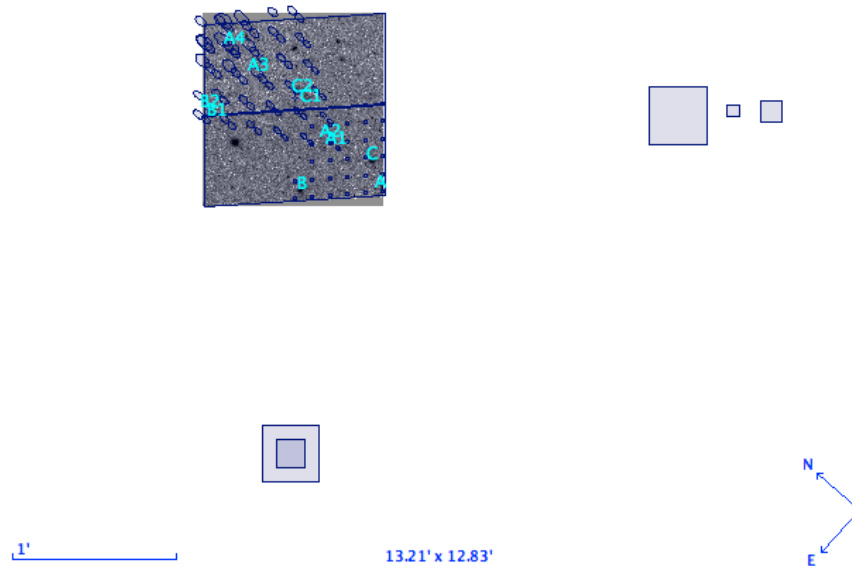
Figure 8: Observers planning their WFC3 UVIS observations should take care to orient the ghost overlay correctly (see text for instructions). The WFC3 UVIS ghost overlay (here for the same image and orientation as the previous figure, but zoomed out 4x) includes NICMOS (three rectangles at 3 o'clock in the diagram) and STIS (two overlapping squares at 6 o'clock) in order to facilitate correct orientation. To produce window ghosts, stars must be in quadrant D, the one in the direction between NICMOS and STIS on this diagram; the ghosts will be diagonally across, generally in quadrant A.
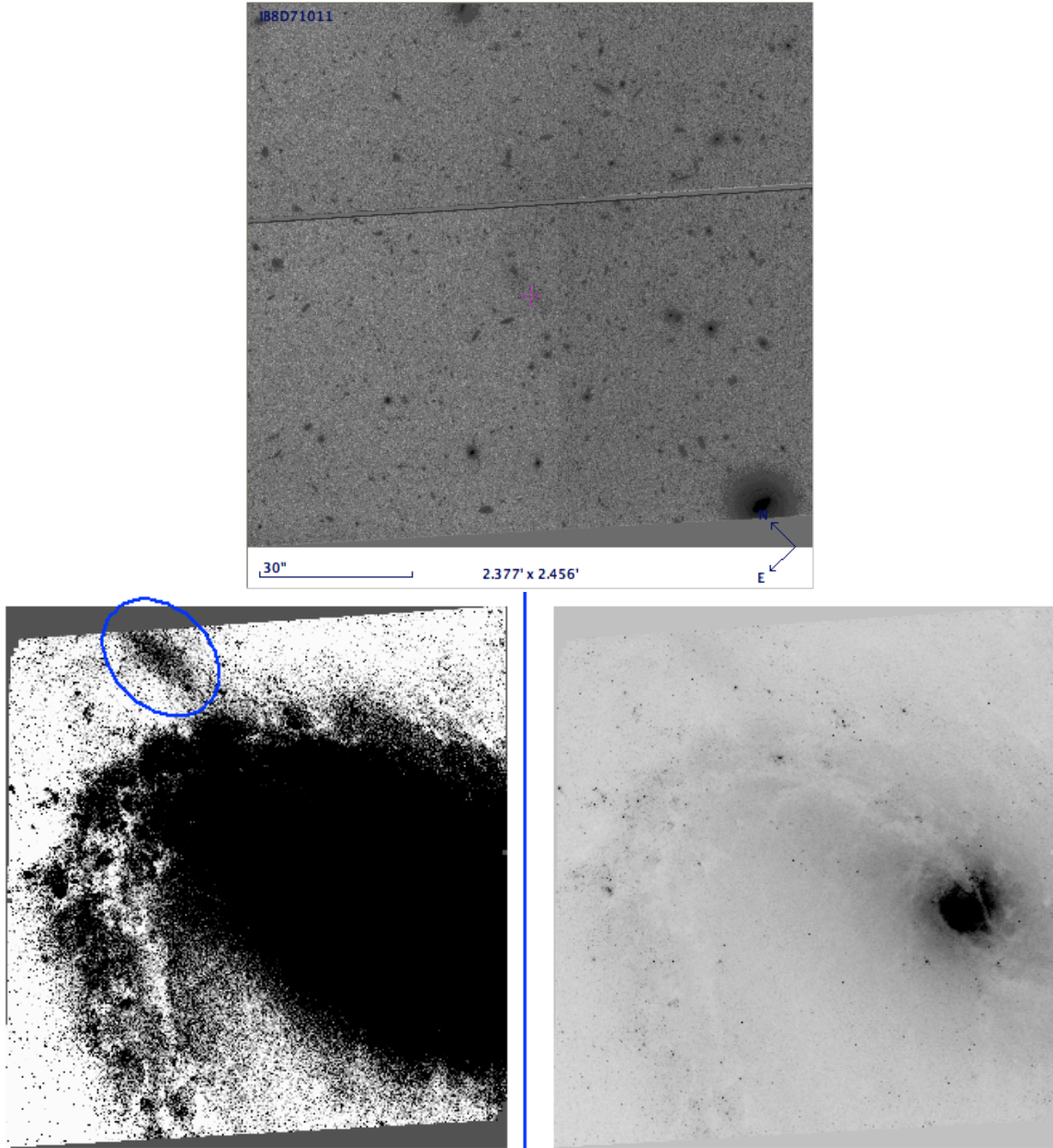
Figure 9: Ghosts visible from non-stellar objects (galaxies). (Top) The galaxy USNOB1 1280-0227695, with an N-band (0.8 micron) integrated brightness of 15.26 mag is visible in the lower right quadrant (near the gnomon). Based upon examination of window-ghost overlays (not shown here), we believe two ghosts of that galaxy cause the faint smudges just barely visible above the background to the left and right of (and similar in size to) the magenta + symbol. Exposure IB8D71011, also from program 11700, is a 1815 second exposure through F606W aimed at RA: 10 30 51.35, Dec: +38 03 39.84. The display has a logarithmic stretch. (Bottom, left and right) The galaxy M83 exhibits a ghost (inside the blue ellipse in the left image) of its bright extended nucleus (visible in the right image) on its own spiral arm. Image IB6W62060 from program 11360 (O'Connell, P.I.) is a 1213 second exposure through F814W.
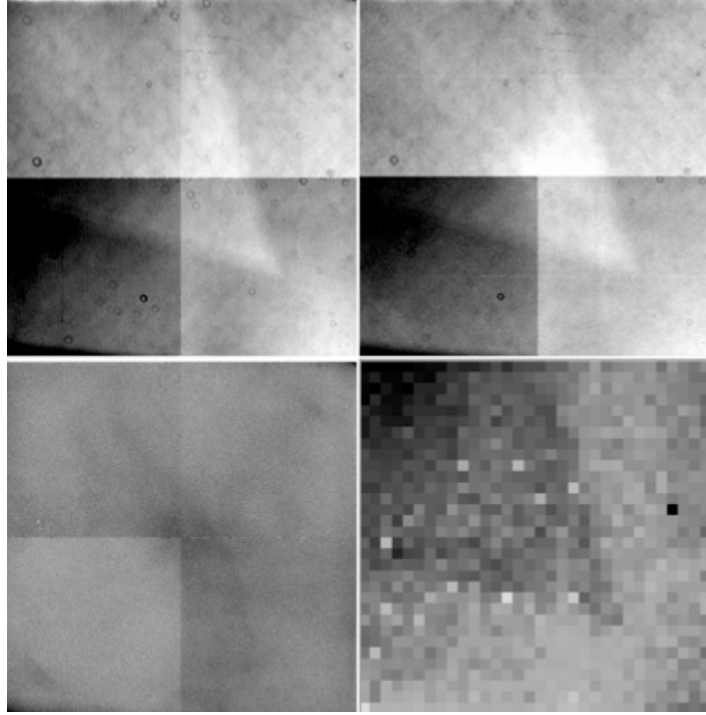
Figure 10: The wedge-shaped feature is evident in flat fields (Pavlosky et al. 2011). Clockwise from upper left, the four panels are as follows: a) the F606W ground flat, obtained with CASTLE illumination and b) an Earth flat from program 11914 (Pavlovsky p.c.). Their ratio (panel c) gives an indication of the low-frequency sensitivity corrections, aside from the window ghosts, which must be applied to the ground flats for observations of sparse fields that do not fully illuminate the detector. Panel d represents a 32x32 matrix solution of the low-frequency residual sensitivity, based on dithered observations of stars and indicating that the flare (which is present in the ground flats) does not represent the detector QE and therefore must be removed from the flat fields. (Mack, p.c.). The wedge-shaped feature is most evident in the lower-right quadrant of the focal plane (except in panel c where the division cancels it out) where its vertex is approximately in the center of that quadrant. In the lower-right quadrant of the ground flats, we (barely) see two levels of brightness within the wedge near the vertex, as predicted by the simulation (Figure 3). Based upon Figure 3, ghosts 3 and 4 should produce two "mini-wedges," one with a vertex near the center of the upper left quadrant and the other with its vertex approximately halfway between the quadrant's center and its upper-left corner. The "mini-wedges" of ghosts 3 and 4 are much less prominent compared to the wedge caused by the superposition of ghosts 1 and 2. We attribute the lack of prominence to the combination of factors: the "mini-wedges" are smaller (they have ~3 or ~6 times shorter edges than the main wedge); their edges are duller (i.e. less sharp, due to the larger size of the defocused ellipse); and their superposition occurs in two separate distinct steps that are spatially much more separated than the main wedge's; and also their surface brightnesses are expected to be slightly less due to the reflective losses that create ghosts 1 and 2. Because the standard stars used to compute the WFC3 zeropoints were obtained in various locations in amplifier A, these 4 wedges must be removed from the flats before computing their photometry. For the ground and Earth flats, gradients within the quadrants (parallel to the diagonal from upper left to lower right), are due to pixel area corrections, which are ~3.5% across each quadrant. The reader should ignore the DC offset of each quadrant (most evident in the lower left quadrant) caused by the CALWFC3 pipeline at the time these diagrams were constructed.
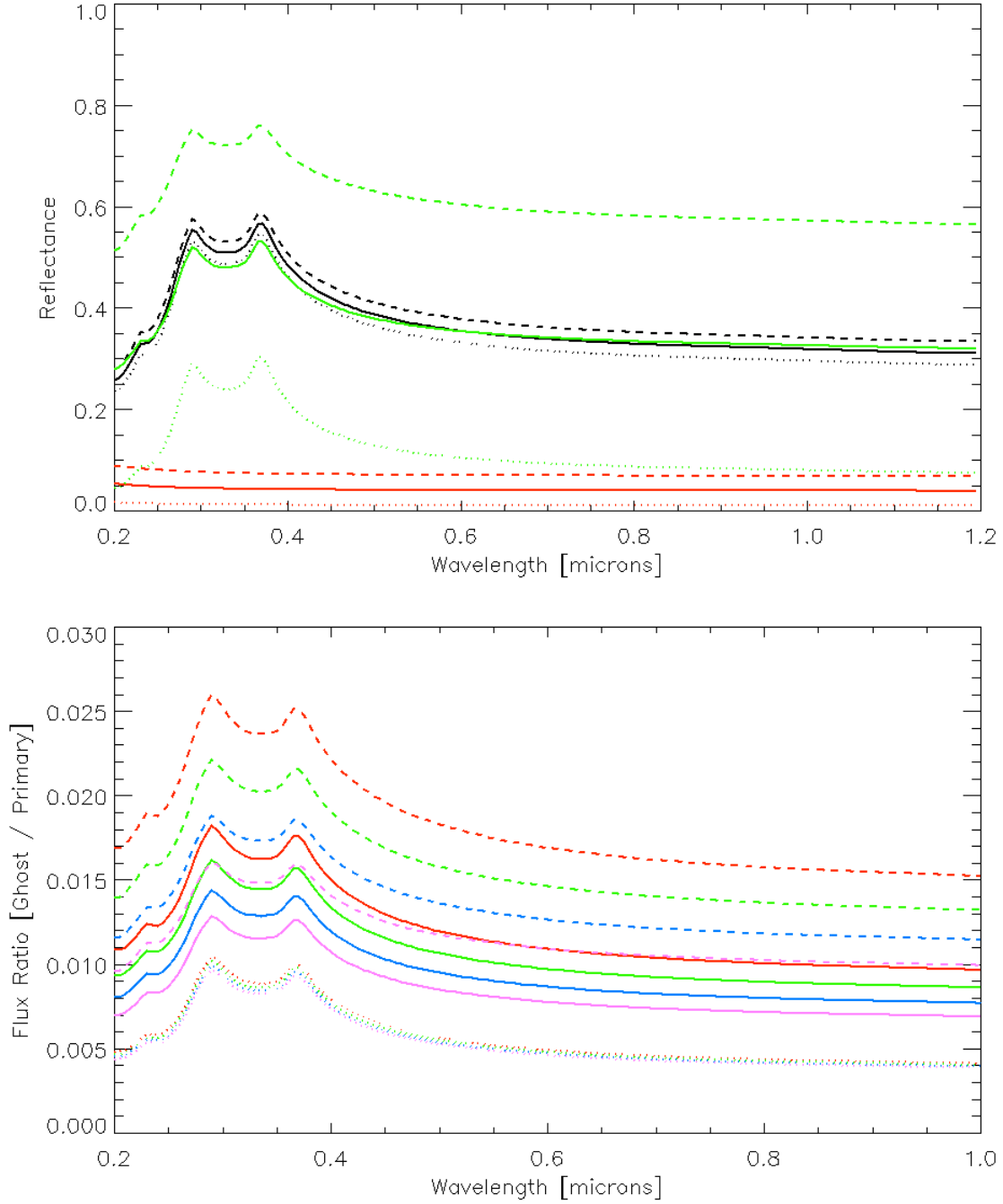
Figure 11: **The wavelength dependence of the reflectance from surfaces (above) and the implied ghost-to-primary-image ratio (below). Linear polarization is indicated as perpendicular (dashed), parallel (dotted), and their mean (solid). For reflectance, color indicates which reflection: silicon at θ (black), fused silica at 2θ (red), and silicon at 3θ (green). For the flux ratio, color indicates which ghost: ghosts 1, 2, 3, and 4 are red, green, blue, and magenta. The curves are directly from the model and are tabulated in Table A1, except that in columns 5-7 of Table A1 the ghost-to-primary-image ratios from the model (here in lower plot in red) have been scaled by 0.7 in order to match observations. The model does not include the anti-reflection coatings on the actual surfaces.**